LETTERS
https://doi.org/10.1038/s41563-021-01077-1

nature materials

Atomic-scale visualization of electronic fluid flow

Xiaolong Liu[1,6], Yi Xue Chong[1,6], Rahul Sharma[1,2] and J. C. Séamus Davis[1,3,4,5] ✉

The most essential characteristic of any fluid is the velocity field, and this is particularly true for macroscopic quantum fluids[1]. Although rapid advances[2–7] have occurred in quantum fluid velocity field imaging[8], the velocity field of a charged superfluid—a superconductor—has never been visualized. Here we use superconducting-tip scanning tunnelling microscopy[9–11] to image the electron-pair density and velocity fields of the flowing electron-pair fluid in superconducting $NbSe_2$. Imaging of the velocity fields surrounding a quantized vortex[12,13] finds electronic fluid flow with speeds reaching 10,000 km h^{-1}. Together with independent imaging of the electron-pair density via Josephson tunnelling, we visualize the supercurrent density, which peaks above 3×10^7 A cm^{-2}. The spatial patterns in electronic fluid flow and magneto-hydrodynamics reveal hexagonal structures coaligned to the crystal lattice and quasiparticle bound states[14], as long anticipated[15–18]. These techniques pave the way for electronic fluid flow visualization studies of other charged quantum fluids.

Visualization of quantum fluid dynamics is now at the research frontier. Molecular tagging velocimetry[2–5] allows visualization of the velocity field $\mathbf{v}(\mathbf{r})$ in superfluid ^{4}He for studies of obstacle quantum turbulence[2], quantized vortex dynamics[3] and thermal-counterflow quantum turbulence[4]. In superfluid ^{3}He, effects of the Galilean energy-boosted quasiparticle spectrum of the moving superfluid are used to study quantized vortex rings and superfluid turbulence[6]. In atomic-vapour superfluids such as ^{23}Na, the phonon Doppler shift allows superflow $\mathbf{v}(\mathbf{r})$ to be imaged[7], while the circulation quanta in turbulent superflow are visualized using Bragg scattering[8]. However, although the hydrodynamics of electron fluids have recently become of intense interest[19–23], direct atomic-scale visualization of electron fluid flow remains elusive.

An electron-pair fluid in a macroscopic quantum state with the many-body wavefunction $\psi(\boldsymbol{r}) = \sqrt{n_S(\boldsymbol{r})}e^{i\theta(\boldsymbol{r})}$ is nominally a superconductor[1]. Here $n_S(\mathbf{r})$ is the number density of condensed electron pairs with charge $-2e$ at location $\boldsymbol{r}$, $\rho_S(\boldsymbol{r}) \equiv -2en_S(\boldsymbol{r})$ is the electron-pair density and $\theta(\mathbf{r})$ is the macroscopic quantum phase. If $\theta(\mathbf{r})$ varies spatially, this implies that the superfluid is moving relative to the host crystal with superfluid velocity $\mathbf{v}_S(\mathbf{r})$ such that $\hbar\nabla\theta(\mathbf{r}) = 2m\mathbf{v}_S(\mathbf{r}) - 2e\mathbf{A}(\mathbf{r})$, where $\hbar$ is the reduced Planck constant; $2m$ is the effective mass of an electron-pair and $\mathbf{A}(\mathbf{r})$ is the vector potential of magnetic fields $\mathbf{B}(\mathbf{r})$ due to supercurrent density $\mathbf{j}_S(\mathbf{r})$, where $\mathbf{j}_S(\mathbf{r}) \equiv \rho_S(\mathbf{r})\mathbf{v}_S(\mathbf{r})$. The quantum fields $\psi(\mathbf{r})$ and $\rho_S(\mathbf{r})$ and associated electronic fluid flow fields $\mathbf{v}_S(\mathbf{r})$ and $\mathbf{j}_S(\mathbf{r})$ are characteristics of the two-particle condensate and not of the Bogoliubov quasiparticle excited states[1]. And, while such quasiparticles have been visualized in a wide variety of single-electron tunnelling experiments, few visualizations of $\rho_S(\mathbf{r})$ have been achieved[9–11] and none whatsoever of $\mathbf{v}_S(\mathbf{r})$ or $\mathbf{j}_S(\mathbf{r})$ have been achieved at the atomic scale.

The magneto-hydrodynamics of superconductive flow has an intricate phenomenology. First, there is the Meissner effect wherein an external magnetic field $\mathbf{B}$ is completely excluded from the superconductive bulk except for a layer with a thickness of the London penetration depth[1] λ or within topological defects of the order parameter. Second, the electron-pair density $\rho_S(\mathbf{r})$ is itself influenced by the superfluid velocity $\mathbf{v}_S(\mathbf{r})$, in the simplest case as $\rho_S(v_S) \approx \rho_S(0)(1 - v_S^2/v_0^2)$ for samples of thickness $t < \xi$, where ξ is the coherence length and $v_0 = \hbar/2m\xi$. Finally, in the reference frame, which is stationary with respect to the superfluid, each Bogoliubov quasiparticle state $|\mathbf{k}\rangle$ exhibits the standard energy spectrum $E_{\boldsymbol{k}} = \pm\sqrt{\varepsilon_{\boldsymbol{k}}^2 + \Delta_S^2}$ (Fig. 1a, red). Here $\varepsilon_{\mathbf{k}}$ is the normal-state band structure referenced to the Fermi energy and Δ_S is the electron-pairing order parameter. But in the laboratory or crystal frame where the superfluid has velocity $\mathbf{v}_S(\mathbf{r}) \neq 0$, each quasiparticle $|\mathbf{k}\rangle$ receives a Galilean energy boost[6,24–26], yielding a new quasiparticle spectrum $E'_{\boldsymbol{k}} = \pm\sqrt{\varepsilon_{\boldsymbol{k}}^2 + \Delta_S^2} + \hbar\mathbf{k}\cdot\mathbf{v}_S(\mathbf{r})$ (Fig. 1a, blue). Thus, in principle, the flow field of an electronic fluid could be visualized by imaging

$$\mathbf{v}_S(\mathbf{r}) \cdot \mathbf{n}_{\mathbf{k}_F} = (E'_{\mathbf{k}_F}(\mathbf{r}) - E_{\mathbf{k}_F}(\mathbf{r}))/\hbar k_F \equiv \delta E_{\mathbf{k}_F}(\mathbf{r})/\hbar k_F \quad (1)$$

where $\mathbf{n}_{\mathbf{k}_F}$ is the unit vector of the Fermi wavevector $\mathbf{k}_F$, and $\delta E_{\mathbf{k}_F}$ is the change of energy at $\mathbf{k}_F$. Therefore, the electronic fluid flow speed can be determined as

$$v_S = \max(\delta E_{\mathbf{k}_F})/\hbar k_F \equiv \delta E_{k_F}/\hbar k_F \quad (2)$$

for simple circular Fermi surfaces.

In practice, however, use of equation (2) presents a number of technical barriers. These include requirements to achieve imaging of the electron-pair density $\rho_S(\mathbf{r})$ and microelectronvolt-resolution imaging of $\delta E_{\mathbf{k}_F}(\mathbf{r})$. Millikelvin scanning tunnelling microscopy (STM) using superconductor–insulator–superconductor (SIS) junctions has recently emerged as a key approach. In the Josephson tunnelling of electron pairs between a superconducting tip and sample[9–11,27,28], the Josephson critical current is $I_J \propto \sqrt{\rho_T\rho_S}/R_N$ as $T \to 0$, where T is temperature, ρ_T is the constant electron-pair density in the scan tip, and R_N is the normal-state resistance of the Josephson junction. Therefore, scanned Josephson tunnelling microscopy (SJTM) imaging of $I_J^2(\mathbf{r})R_N^2(\mathbf{r}) \propto \rho_S(\mathbf{r})$ should allow atomic-scale visualization of the electron-pair density[9–11]. Most SJTM systems operate at temperatures $k_BT > E_J = \Phi_0 I_J/2\pi$ (k_B is the Boltzmann constant; E_J is the Josephson energy; Φ_0 is the magnetic flux quantum) such that electron-pair tunnelling exhibits a phase-diffusive steady-state current[29] $I_P(V_J) = \frac{1}{2}I_J^2 ZV_J/\left(V_J^2 + V_C^2\right)$ (Fig. 1b). V_J is the phase-diffusive voltage across the junction; Z is its high-frequency impedance; and $V_C = 2eZk_BT/\hbar$. Thus the zero-bias

[1]Department of Physics, Cornell University, Ithaca, NY, USA. [2]Department of Physics, University of Maryland, College Park, MD, USA. [3]Department of Physics, University College Cork, Cork, Ireland. [4]Max-Planck Institute for Chemical Physics of Solids, Dresden, Germany. [5]Clarendon Laboratory, University of Oxford, Oxford, UK. [6]These authors contributed equally: Xiaolong Liu, Yi Xue Chong. ✉e-mail: jcseamusdavis@gmail.com

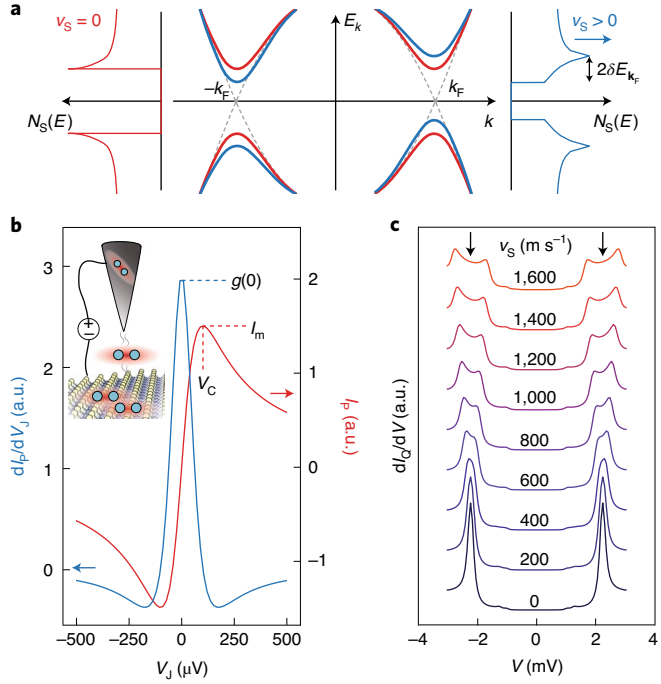

Fig. 1 | Model of quasiparticle and electron-pair tunnelling. a, Schematic spectrum $E_{\mathbf{k}}$ and density of states $N_S(E)$ of Bogoliubov quasiparticles with electronic fluid velocity $v_S = 0$ (red) and $v_S \neq 0$ (blue) such that $\delta E_{\mathbf{k}_F} = 0.4\Delta_S$. **b**, Phase-diffusive Josephson electron-pair spectrum dI_P/dV_J (blue) and $I_P(V_J)$ (red). The maximum Josephson current is I_m at voltage $V_J = V_C$. The zero-bias conductance is $g(0)$. Inset: schematic showing the tunnelling of electron-pairs between the tip and sample. **c**, A series of simulated spectra $g(V,\Delta_S = 1\,\text{meV},\delta E_{\mathbf{k}_F}) \equiv dI_Q/dV$ in the SIS configuration schematic of Bogoliubov quasiparticle tunnelling for electronic fluid flow with different speeds $v_S = \delta E_{\mathbf{k}_F}/\hbar k_F$. A comparison between these pedagogical spectra and experimental data should not yield any specific conclusions about v_S in $NbSe_2$, given this simplified pedagogical presentation. Instead, the fitting of experimental spectra with realistic modelling of $NbSe_2$ is required (Supplementary Notes 3 and 4).

differential conductance is $g(0) \equiv (dI_P/dV_J)|_{V=0} \propto I_J^2$ (Fig. 1b) so that[9–11]

$$\rho_S(\mathbf{r}) \propto g(\mathbf{r},0) R_N^2(\mathbf{r}) \tag{3}$$

(Supplementary Note 1). For quasiparticle tunnelling between the same tip and sample, the quasiparticle current as $T \to 0$ is

$$I_Q(V) \propto \int_0^{eV} N_T(\epsilon - eV)\, N_S(\epsilon) d\epsilon \tag{4}$$

where N_T and N_S are the quasiparticle density-of-states of the tip and sample, respectively, ϵ is energy and V is sample voltage. This yields an SIS tunnelling spectrum

$$g(V) \equiv \frac{dI_Q}{dV} \propto \frac{d}{dV} \int_0^{eV} N_T(\epsilon - eV)\, N_S(\epsilon) d\epsilon \tag{5}$$

Here $N_{T,S}(\varepsilon)$ can be determined from the quasiparticle Green's function

$$G(\mathbf{k}, \epsilon, \Delta_{T,S}) \equiv (\epsilon + i\delta + \varepsilon_{\mathbf{k}}) / \left((\epsilon + i\delta)^2 - \varepsilon_{\mathbf{k}}^2 - \Delta_{T,S}^2\right) \tag{6}$$

with scattering rate $\delta/\hbar$. Thus

$$N_{T,S}(\epsilon) = -\int d\mathbf{k} \frac{2}{\pi} \Im(G(\mathbf{k}, \epsilon, \Delta_{T,S})) \tag{7}$$

where $\Im$ denotes taking the imaginary part, and the tip and sample have superconducting energy gaps Δ_T and Δ_S, respectively. The SIS spectrum $g(V)$, being the convolution of two superconducting coherence peaks diverging at $V = \pm\Delta_T/e$ and $V = \pm\Delta_S/e$, is then an extremely sharply peaked function at $V = \pm(\Delta_T + \Delta_S)/e$ (bottom spectrum in Fig. 1c), and is dominated by states at $\mathbf{k} = \mathbf{k}_F$ (Fig. 1a). However, an electron-pair fluid flowing through the sample with velocity $\mathbf{v}_S$ modifies $N_S(\varepsilon)$ due to the Galilean energy boost of $\delta E_{\mathbf{k}} = \hbar\mathbf{k} \cdot \mathbf{v}_S$. In this case[30]

$$N_S(\epsilon, \delta E_{k_F}, \Delta_S) = -\int d\mathbf{k} \frac{2}{\pi} \Im(G(\mathbf{k}, \epsilon - \delta E_{\mathbf{k}}, \Delta_S)) \tag{8}$$

so that $g(V, \Delta_S, \delta E_{k_F})$ becomes a quite complex function around $V = \pm(\Delta_T + \Delta_S)/e$. Figure 1c shows simulated $g(V, \Delta_S, \delta E_{k_F})$ spectra derived from equation (5) for a fixed $\Delta_T = 1$ meV and $\Delta_S = 1.2$ meV and for a variety of superfluid velocities $0 < v_S < 1{,}600$ m s^{-1}. It is the ultra-high-energy-resolution SIS tunnelling (Supplementary Fig. 1) that allows the Galilean energy boosts $\delta E_{\mathbf{k}_F}$ to become manifest as splitting of the sharp maxima in $g(V,\Delta_S,\delta E_{\mathbf{k}_F})$ at $V = \pm(\Delta_T + \Delta_S)/e$ (arrows in Fig. 1c). Note that Fig. 1c is pedagogical, designed to illustrate the isolated effects of Galilean energy boosts by keeping Δ_S constant in all spectra, and that equation (8) yields far more complex $g(V, \Delta_S, \delta E_{\mathbf{k}_F})$ spectra for real materials and variable Δ_S. Nonetheless, due to the different roles played by $\Delta_S(\mathbf{r})$ and $\delta E_{\mathbf{k}_F}$ in equation (8), SIS imaging of $g(\mathbf{r},V)$ with sufficient spatial and energy resolution near $V = \pm(\Delta_T + \Delta_S)/e$ should allow visualization of both $\Delta_S(\mathbf{r})$ and $\mathbf{v}_S(\mathbf{r})$ (Supplementary Note 2). The overall challenge has been to achieve $g(\mathbf{r},0)$ and $\delta E_{\mathbf{k}_F}(\mathbf{r})$ imaging adequate to yield simultaneous, two-dimensional visualization of $\rho_S(\mathbf{r})$, $\mathbf{v}_S(\mathbf{r})$ and thus $\mathbf{j}_S(\mathbf{r})$.

To explore these challenges, we use 2H-$NbSe_2$, whose superconductive critical temperature is $T_C \approx 7.2$ K and anisotropic energy gap is $\Delta_S(\mathbf{k}) \approx \Delta_0(0.8 + 0.2\cos(6\arctan(k_y/k_x)))$, where Δ_0 is a parameter, and k_x and k_y are wavevectors along two normal directions (Supplementary Note 3). This material has a hexagonal layered structure with Se–Se separation d (Supplementary Fig. 2) and a coexisting charge density wave state with in-plane wavevectors $\mathbf{Q}_i \approx \{(1,0); (1/2, \sqrt{3}/2); (-1/2, \sqrt{3}/2)\}\, 2\pi/3a_0$ where $a_0 = \sqrt{3}d/2$. Figure 2a shows the topographic image of the $NbSe_2$ surface with a magnetic field $B = 50$ mT applied to generate a very low density of quantized vortices.

A rapidly flowing electron-pair fluid surrounds each vortex core[12,13] within which quasiparticle states become bound[14,17]. But the iconic Abrikosov model[12] cannot predict the effects on this flow field of crystal fields, or of multiple electronic bands and their anisotropic superconducting energy gaps. Thus, the quantum magneto-hydrodynamic phenomenology of a superconductive vortex has long been studied using the Eilenberger equations for the Green's functions[15], or the Bogoliubov-de Gennes equations[16–18]. For $NbSe_2$ specifically, self-consistent solutions of the Bogoliubov-de-Gennes equations predict that the electron-pair field, fluid velocity and current density outside the core should all be hexagonal and, moreover, aligned to both the crystal axes and the symmetry axes of quasiparticle bound states[17,18]. But it has never been possible to explore any of these predictions because no techniques whatsoever existed for electronic fluid flow visualization.

To visualize electron-pair fluid flow around quantum vortices, we prepare Nb STM tips by field emission on a Nb target, establishing atomic resolution; typically $\Delta_T \approx 1$ meV, a value that is unperturbed under small magnetic fields (Supplementary Fig. 3). Then, in the same field of view (FOV) as Fig. 2a, the vortex core

is revealed by visualizing the quasiparticle bound states[14] that vanish exponentially with decay constant ξ for $r>\xi$, by measuring $g(\mathbf{r},\Delta_T/e)$ at $T=290$ mK (Fig. 2b). Subsequently we set the origin of coordinates $\mathbf{r}=(0,0)$ at the symmetry point of the vortex core. Next, a complete set of SIS quasiparticle spectra $g(\mathbf{r},V)$ spanning the range $-3\,\mathrm{mV}<V<3\,\mathrm{mV}$ is measured in the same FOV of Fig. 2a,b at constant $R_N(\mathbf{r})=1\,\mathrm{M\Omega}$ and $T=290$ mK (Supplementary Note 2). Figure 2c shows the typical SIS spectrum $g(r\to\infty,V)$ with sharp convoluted coherence peaks at $V=\pm(\Delta_T+\Delta_0)/e$, along with that of $g(r\to 0,V)$ showing the convolved spectrum of the Nb-tip coherence peaks at $V=\pm(\Delta_T)/e$. Simultaneously, we use SJTM to measure the electron-pair tunnelling $g(\mathbf{r},0)$ peak, with the results shown in Fig. 2d. The electron-pair tunnelling spectrum as $V\to 0$ is shown in Supplementary Figs. 4 and 5. Finally, it is by combining these techniques that the magneto-hydrodynamics of the electron-pair fluid surrounding the vortex core becomes manifest.

Figure 2e (top panel) shows the measured evolution of these SIS spectra along a radial trajectory $0<r<152$ nm. Here, the colour code represents the intensity of $g(r,V)$, the vertical axis is radius r and the horizontal axis is V. Next, we determine the superconducting order parameter $\Delta_S(\mathbf{r})$ and the Galilean energy boost $\delta E_{\mathbf{k}_F}$ by fitting these measured $g(\mathbf{r},V)$ at each $\mathbf{r}$, to the model $g(V,\Delta_S,\delta E_{\mathbf{k}_F})$ spectra derived from equations (5) and (8). The best fit is identified by finding the least-valued, normalized, root-mean-square deviation (σ_N; Supplementary Note 4). Figure 2e (bottom panel) then shows the evolution of the best-fit $g(V,\Delta_S,\delta E_{\mathbf{k}_F})$ along the same radial trajectory $0<r<152$ nm. The correspondence of experimental $g(r,V)$ (top panel) and fitted $g(V,\Delta_S,\delta E_{\mathbf{k}_F})$ (bottom panel) is excellent. This is exemplified directly in Fig. 2f (Supplementary Fig. 7) using examples of experimental $g(r,V)$ and their best-fit $g(V,\Delta_S,\delta E_{\mathbf{k}_F})$ at the radii indicated by the coloured dashed lines in Fig. 2e. The quality of all the fits in Fig. 2e is quantified by their high coefficients of determination R^2 (Supplementary Figs. 8). Next, the best-fit $g(V,\Delta_S,\delta E_{\mathbf{k}_F})$ at each $\mathbf{r}$ yields $\Delta_0(\mathbf{r})$ and $\delta E_{\mathbf{k}_F}(\mathbf{r})$, as shown in Fig. 2g,h, respectively. The radial dependence of electron-pair density $\overline{\rho}_S(r)$ is then evaluated from an azimuthal average of $\rho_S(\mathbf{r})\propto g(\mathbf{r},0)$ (Fig. 3a), while the radial dependence of $\overline{\Delta_0^2}(r)$ is determined from an azimuthal average of $\Delta_0(\mathbf{r})$ (Fig. 3a), where the bars denote azimuthal average. By fitting $\overline{\rho}_S(r)/\overline{\rho}_S(\infty)$ to $\tanh^2\left(\sqrt{3/8}\frac{r}{\xi}\right)$ (Supplementary Note 5), we obtain an in-plane coherence length $\xi=11$ nm, as expected. Then, with superconducting coherence length $\xi\equiv\hbar^2k_F/\pi m\Delta_0$ and $\Delta_0=1.24$ meV, the Fermi wavevector is $k_F=5.7\times10^8\,\mathrm{m}^{-1}$. Finally, the image of electron-pair fluid velocity is attained as $\mathbf{v}_S(\mathbf{r})\equiv\delta E_{\mathbf{k}_F}(\mathbf{r})/\hbar k_F$. From this, the radial dependence of superfluid speed $\overline{v}_S(r)$ and Galilean energy boost $\overline{\delta E_{k_F}}(r)$ from azimuthal averages of $v_S(\mathbf{r})$ and $\delta E_{\mathbf{k}_F}(\mathbf{r})$ is shown in Fig. 3b, for $30\,\mathrm{nm}\le r\le 140$ nm (beyond the range of influence of quasiparticle states bound in the core; Supplementary Note 4 and Supplementary Fig. 9). Measurements of $v_S(\mathbf{r})$ from different vortices under different magnetic fields and using different SJTM tips yield repeatable results that are quantitatively indistinguishable from those presented here (Supplementary Fig. 10).

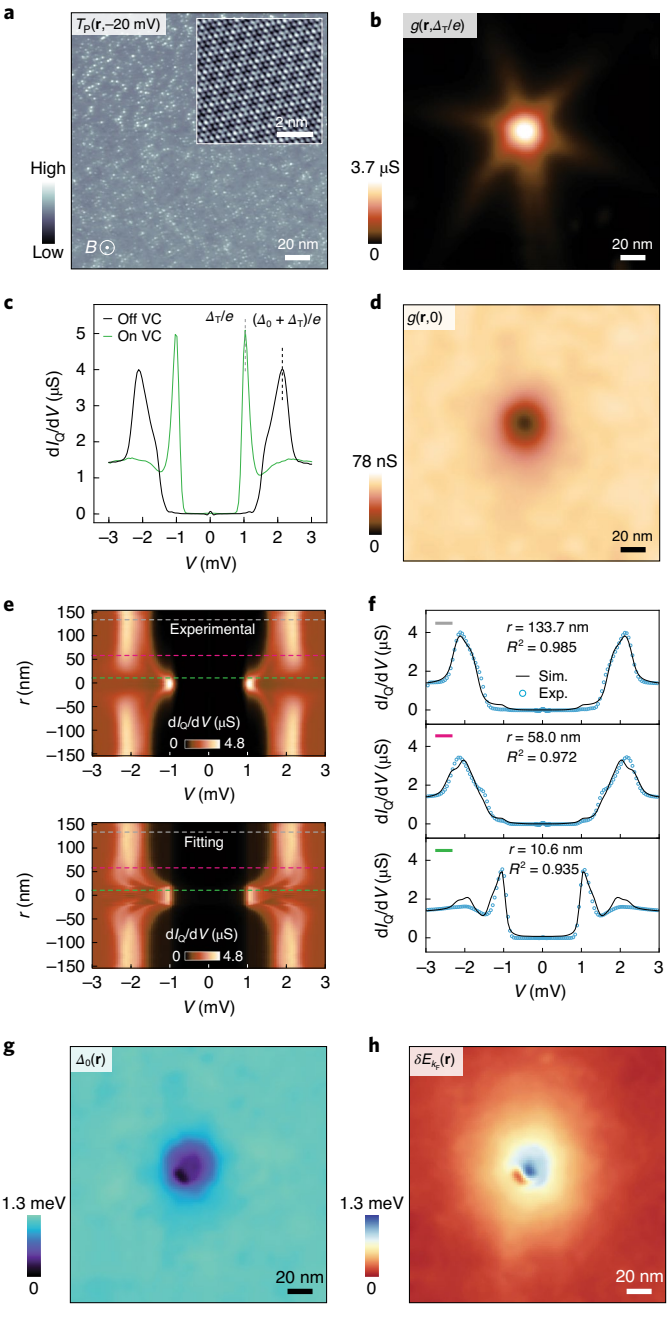

Fig. 2 | Quasiparticle tunnelling and electron-pair tunnelling experiments. Images and spectroscopy of a single vortex, all acquired in the same FOV at $T=290$ mK and with $B=50$ mT applied perpendicular to the surface. Due to SIS tunnelling spectroscopy, an energy resolution of ~20 μeV is achieved throughout these studies. **a**, Measured topography $T_P(\mathbf{r},-20\,\mathrm{mV})$ of studied FOV with inset showing atomically resolved topography under the same tip condition. The white spots are point defects intrinsic to $NbSe_2$. **b**, Measured $g(\mathbf{r},\Delta_T/e)$ revealing the quasiparticle bound states at the vortex core (VC). **c**, Measured quasiparticle dI_Q/dV spectra at $r\to 0$ (green) and $r>100$ nm (black). **d**, Measured $g(\mathbf{r},0)$ of electron-pair tunnelling. **e**, Measured $g(\mathbf{r},V)=dI_Q/dV(\mathbf{r},V)$ spectra for each radius r (top panel). The theoretical $g(V,\Delta_S,\delta E_k)$ spectra that best fit the measured $g(\mathbf{r},V)$ at each radius r (bottom panel). Both panels contain the azimuthally averaged results. Multiple Andreev reflections are ruled out as the origins of any of these spectra features (Supplementary Note 4 and Supplementary Fig. 6). **f**, Examples of fitted $g(V,\Delta_S,\delta E_k)$ spectra at different radii indicated by the coloured dashed lines in **e** with coefficients of determination (R^2) indicated. The fitting quality only significantly decreases for $r\le\xi$ close to the vortex core (Supplementary Figs. 8 and 9). Sim., simulation; Exp., experiment. **g**, Fitted $\Delta_0(\mathbf{r})$ from the measured $g(\mathbf{r},V)$ spectra. **h**, Fitted $\delta E_{\mathbf{k}_F}(\mathbf{r})$ from the measured $g(\mathbf{r},V)$ spectra. The SIS tunnelling scheme makes it possible to image the Galilean energy boost spatially because of its greatly enhanced energy resolution[11] compared to single-electron (non-superconducting-tip) tunnelling at the same temperature. The anomaly near the vortex core is due to a small region of inferior fitting to the experimental spectra. To suppress noise, a Gaussian blur by 1.5 pixels is applied to the raw data to generate **b**, **d**, **g** and **h**. The full data acquisition time for the experiment reported here is around 40 hours.

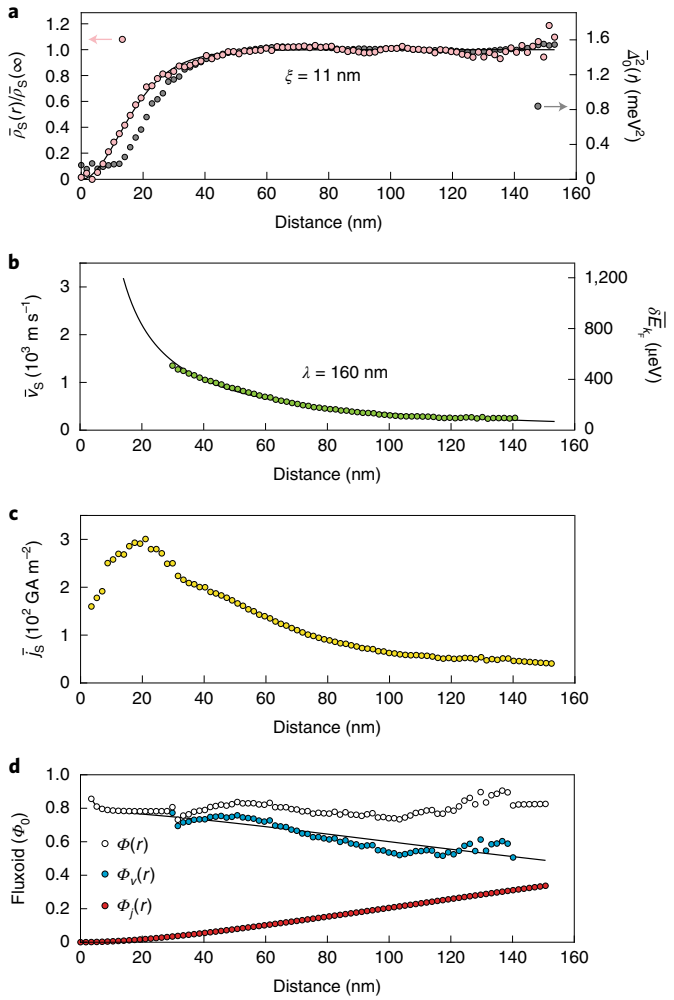

Fig. 3 | Radial dependence of ρ_S, Δ_0^2, v_S, j_S and Φ. **a**, Azimuthal averages of measured $\bar{\rho}_S(r)/\bar{\rho}_S(\infty)$ and $\bar{\Delta}_0^2(r)$. Fitting $\bar{\rho}_S(r)/\bar{\rho}_S(\infty)$ with $\left(\tanh\left(\sqrt{3/8}r/\xi\right)\right)^2$, as shown, results in $\xi = 11$ nm. **b**, Azimuthal average of measured vortical electronic fluid speed $\bar{v}_S(r)$ in the range of $30\,\text{nm} < r < 140\,\text{nm}$. Fitting $\bar{v}_S(r)$ with $\bar{v}_S(r) \approx K_1\left(\frac{r}{\lambda}\right)$ results in $\lambda = 160$ nm. **c**, Azimuthal average of measured vortical current density $\bar{j}_S(r)$. In the range of $30\,\text{nm} < r < 140\,\text{nm}$, $\bar{j}_S(r) = \overline{\rho_S(r)v_S(r)}$ using measured $\rho_S(r)$ in **a** and $v_S(r)$. For $r < 30$ nm and $r > 140$ nm, $\bar{j}_S(r) = \bar{\rho}_S(r)\,\bar{v}_S(r)$ using measured $\rho_S(r)$ and extrapolated $v_S(r)$ from fitting in **b**. **d**, Measured $\Phi_v(r)$, $\Phi_j(r)$ and fluxoid $\Phi(r)$. When summed, $\Phi(r) = \Phi_v(r) + \Phi_j(r) \approx (0.85 \pm 0.1)\Phi_0$. The small deviation from Φ_0 is likely to be due to vortex core bound states (Supplementary Note 4) and modelling $j(\mathbf{r})$ as if around an infinitely long azimuthally symmetric vortex line, while using measured data from the crystal surface where such a line terminates.

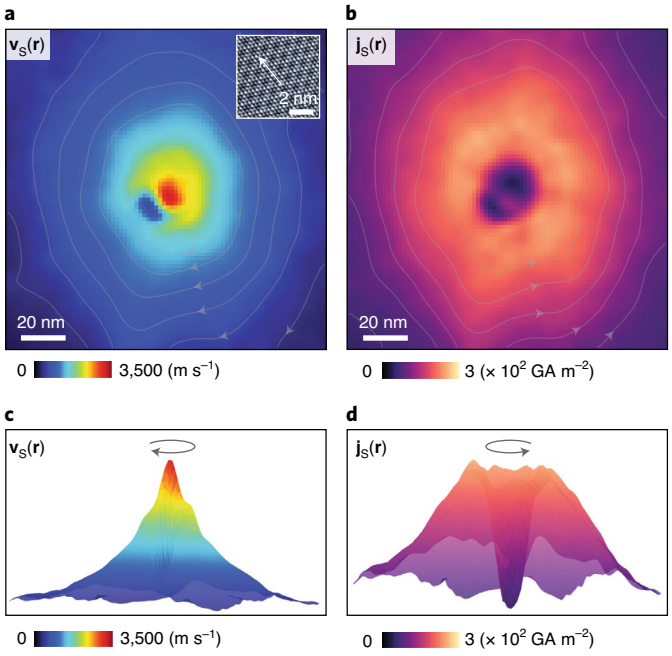

Fig. 4 | Visualizing electronic fluid flow. **a**, Directly measured $\mathbf{v}_S(\mathbf{r})$ without extrapolation with overlaid contour lines from 400 to 1,400 m s^{-1} (or 1,440 to 5,040 km h^{-1}) with 200 m s^{-1} intervals. The white arrow indicates the lattice direction based on the atomic topography image (inset) taken within the FOV (same as Fig. 2a inset). **b**, Directly measured $\mathbf{j}_S(\mathbf{r})$ without extrapolation with overlaid contour lines from 90 to 210 GA m^{-2} with 30 GA m^{-2} intervals. The FOVs in **a** and **b** are 70% of that in Fig. 2a to highlight the vortex. To suppress noise, a Gaussian blur by 1.5 pixels is applied to the raw data to generate **a** and **b**. **c**, Side view of $\mathbf{v}_S(\mathbf{r})$ in a three-dimensional presentation. **d**, Side view of $\mathbf{j}_S(\mathbf{r})$ in a three-dimensional presentation.

Quantitative analysis begins with a comparison between $\bar{\Delta}_0^2(\mathbf{r})$ from fitting SIS $g(\mathbf{r},V)$ spectra, and the independently determined $\bar{\rho}_S(r)$ from SJTM electron-pair tunnelling, finding them in good agreement (Fig. 3a). Because in theory $\rho_S(r) \propto \Delta_0^2(r)$, this observation gives strong confidence in the fitting procedures of the measured SIS $g(V)$ spectra. Next, because of the nearly constant $\rho_S(r)$ in the range of $30\,\text{nm} \le r \le 140\,\text{nm}$, we fit $\bar{v}_S(r) \propto K_1\left(\frac{r}{\lambda}\right)$, where $K_1(x)$ is a first-order modified Bessel function of the second kind (Fig. 3b and Supplementary Note 6). This yields an in-plane penetration depth of $\lambda = 160$ nm and thus anisotropy parameter $\kappa_\perp = \lambda/\xi = 14.5$, in agreement with previous reports (Supplementary Note 3). Using the London penetration depth $\lambda = \sqrt{m/2\mu_0 n_S(\infty)e^2}$, where μ_0 is the vacuum permeability, we estimate that $n_S(\infty) \approx 5.5 \times 10^{26}$ m^{-3} yielding $\rho_S(\mathbf{r}) = -2en_S(\infty)g(\mathbf{r},0)/g(r \gg \xi,0)$. The radial dependence of current density $\bar{j}_S(r)$ as determined from the azimuthal average of $j_S(\mathbf{r}) = \rho_S(\mathbf{r})v_S(\mathbf{r})$ is then shown in Fig. 3c. As $r \to 0$, $\bar{j}_S(r)$ is estimated as $\bar{\rho}_S(r)\bar{v}_S(r)$ by using the extrapolated $\bar{v}_S(r)$ (Fig. 3b). Because in general $\nabla\theta(\mathbf{r}) = (\mathbf{A}(\mathbf{r}) - m\mathbf{v}_S(\mathbf{r})/e)(-2\pi/\Phi_0)$, the quantum phase winding around the vortex core at radius r is

$$\Theta(r) \equiv \left|\oint \nabla\theta(\mathbf{r}) \cdot \mathrm{d}\mathbf{l}\right| = \frac{2\pi}{\Phi_0}\left(\iint \mathbf{B} \cdot \mathrm{d}\mathbf{s} - \oint \frac{m\mathbf{v}_S(\mathbf{r})}{e} \cdot \mathrm{d}\mathbf{l}\right) \quad (9)$$

where $\mathbf{s}$ and $\mathbf{l}$ denote areas and paths. The topological constraint $\Theta = 2\pi$ then generates fluxoid quantization

$$\Phi \equiv \iint \mathbf{B} \cdot \mathrm{d}\mathbf{s} - \oint \frac{m\mathbf{v}_S(\mathbf{r})}{e} \cdot \mathrm{d}\mathbf{l} = \Phi_0. \quad (10)$$

From our measured $\bar{v}_S(r)$ and $\bar{\rho}_S(r)$, these two contributing terms yield

$$\Phi_v(r) \equiv -\oint \frac{m\bar{\mathbf{v}}_S(r)}{e} \cdot \mathrm{d}\mathbf{l} \quad (11A)$$

$$\Phi_j(r) \equiv \iint \mathbf{B} \cdot \mathrm{d}\mathbf{s} = 2\pi \int_0^r r_0 \mathrm{d}r_0 \int_{r_0}^{\infty} \mu_0 \bar{v}_S(r')\,\bar{\rho}_S(r')\,\mathrm{d}r' \quad (11B)$$

where equation (11B) is derived using Ampere's Law with azimuthal symmetry. The measured $\Phi_v(r)$ and $\Phi_j(r)$ are shown in

Fig. 3d as blue and red circles, respectively. As anticipated, they evolve in opposite directions such that their sum results in the virtually radius-independent value $\Phi(r) = (0.85 \pm 0.1)\Phi_0$ (white circles in Fig. 3d). Together with the high SIS spectra fitting quality ($R^2 = 0.96$, $\sigma_N \approx 5\%$; Supplementary Figs. 8 and 9), the close matching of $\overline{\Delta}_0^2(r)$ with $\bar{\rho}_S(r)$ (Fig. 3a) and the agreement between mesured ξ, λ and $\kappa_\perp$ values and the literature values (Supplementary Note 3), these observations demonstrate the validity and internal consistency in the techniques used to visualize and quantify $\Delta_S(\mathbf{r})$, $\rho_S(\mathbf{r})$,$\mathbf{v}_S(\mathbf{r})$ and $\mathbf{j}_S(\mathbf{r})$.

Directly imaged flow configurations $\mathbf{v}_S(\mathbf{r})$ and $\mathbf{j}_S(\mathbf{r})$ for the quantum vortex of $NbSe_2$ are shown in Fig. 4a,b, respectively (three-dimensional representations are shown in Fig. 4c,d). While measured electron-pair fluid speeds diverge to $v_S(\mathbf{r}) > 2{,}800\,\mathrm{m\,s^{-1}}$ ($>10{,}000\,\mathrm{km\,h^{-1}}$) as $r \to 0$, $j_S(\mathbf{r})$ initially rises but is driven to zero by falling $\rho_S(\mathbf{r})$ so that peak values reach approximately $3 \times 10^7\,\mathrm{A\,cm^{-2}}$. Evaluation of the fluxoid from measured $\mathbf{v}_S(\mathbf{r})$ and $\mathbf{j}_S(\mathbf{r})$ yields a value slightly less than Φ_0, perhaps because of deviations of the magnetic field direction away from the z axis due to the surface termination of $\mathbf{j}_S(\mathbf{r})$. More importantly, the electron-pair fluid velocity field $\mathbf{v}_S(\mathbf{r})$ exhibits a distinct hexagonal symmetry aligned to the crystal axis (Fig. 4a), and this phenomenon is more pronounced in $\mathbf{j}_S(\mathbf{r})$ (Fig. 4b and Supplementary Fig. 11). Moreover, the image of fitted $\Delta_S(\mathbf{r})$ shows the hexagonal symmetry (Fig. 2g and Supplementary Fig. 12). Hence, surrounding each $NbSe_2$ vortex core, the imaging reveals an electron-pair potential, a velocity field for the electron-pair fluid flow and a pattern of current density, all of which are hexagonal. They are all coaligned to both the crystal axes and the quasiparticle bound states (Fig. 2b and Supplementary Fig. 12), as long anticipated[15–18].

Overall, by introducing techniques for simultaneous imaging of the $\mathbf{v}_S(\mathbf{r})$, $\rho_S(r)$ and thus $\mathbf{j}_S(\mathbf{r})$ of a flowing electronic fluid, we visualize the atomic-scale magneto-hydrodynamics surrounding a superconductive quantized vortex core (Fig. 4), finding it in excellent agreement with long-standing theories. Such visualization capabilities make possible novel research prospects including visualizing flowing electronic fluids surrounding vortices in topological and cuprate superconductors, in the surface currents generated by the superconductive Meissner effect, in chiral edge currents of topological superconductors and in the viscosity-influenced currents of ultra-metals (Supplementary Note 7). More generally, because visualization is a powerful and flexible tool for scientific research in general, the capability to visualize flowing electronic fluids that we have introduced here has wide potential.

Online content

Any methods, additional references, Nature Research reporting summaries, source data, extended data, supplementary information, acknowledgements, peer review information; details of author contributions and competing interests; and statements of data and code availability are available at https://doi.org/10.1038/s41563-021-01077-1.

Received: 18 January 2021; Accepted: 12 July 2021;
Published online: 30 August 2021

References

1. Leggett, A. J. *Quantum Liquids: Bose Condensation and Cooper Pairing in Condensed-Matter Systems* (Oxford Univ. Press, 2006).
2. Zhang, T. & Van Sciver, S. W. Large-scale turbulent flow around a cylinder in counterflow superfluid ^{4}He (He(II)). *Nat. Phys.* **1**, 36–38 (2005).
3. Bewley, G. P., Lathrop, D. P. & Sreenivasan, K. R. Visualization of quantized vortices. *Nature* **441**, 588 (2006).
4. Guo, W. et al. Visualization study of counterflow in superfluid ^{4}He using metastable helium molecules. *Phys. Rev. Lett.* **105**, 045301 (2010).
5. Guo, W. et al. Visualization of two-fluid flows of superfluid helium-4. *Proc. Natl Acad. Sci. USA* **111**, 4653–4658 (2014).
6. Fisher, S. N. et al. Andreev reflection, a tool to investigate vortex dynamics and quantum turbulence in ^{3}He-B. *Proc. Natl Acad. Sci. USA* **111**, 4659–4666 (2014).
7. Kumar, A. et al. Minimally destructive, Doppler measurement of a quantized flow in a ring-shaped Bose–Einstein condensate. *N. J. Phys.* **19**, 025001 (2016).
8. Seo, S. W. et al. Observation of vortex-antivortex pairing in decaying 2D turbulence of a superfluid gas. *Sci. Rep.* **7**, 4587 (2017).
9. Hamidian, M. H. et al. Detection of a Cooper-pair density wave in $Bi_2Sr_2CaCu_2O_{8+x}$. *Nature* **532**, 343–347 (2016).
10. Cho, D. et al. A strongly inhomogeneous superfluid in an iron-based superconductor. *Nature* **571**, 541–545 (2019).
11. Liu, X., Chong, Y. X., Sharma, R. & Davis, J. C. S. Discovery of a Cooper-pair density wave state in a transition-metal dichalcogenide. *Science* **372**, 1447–1452 (2021).
12. Abrikosov, A. A. The magnetic properties of superconducting alloys. *J. Phys. Chem. Solids* **2**, 199–208 (1957).
13. Rosenstein, B. & Li, D. Ginzburg-Landau theory of type II superconductors in magnetic field. *Rev. Mod. Phys.* **82**, 109–168 (2010).
14. Hess, H. F., Robinson, R. B. & Waszczak, J. V. Vortex-core structure observed with a scanning tunneling microscope. *Phys. Rev. Lett.* **64**, 2711–2714 (1990).
15. Klein, U. Microscopic calculations on the vortex state of type II superconductors. *J. Low. Temp. Phys.* **69**, 1–37 (1987).
16. Norman, M. R. Mean-field superconductivity in a strong magnetic field. *Physica C* **196**, 43–47 (1992).
17. Gygi, F. & Schlüter, M. Self-consistent electronic structure of a vortex line in a type-II superconductor. *Phys. Rev. B* **43**, 7609–7621 (1991).
18. Rainer, D., Sauls, J. A. & Waxman, D. Current carried by bound states of a superconducting vortex. *Phys. Rev. B* **54**, 10094–10106 (1996).
19. Bandurin, D. A. et al. Negative local resistance caused by viscous electron backflow in graphene. *Science* **351**, 1055–1058 (2016).
20. Crossno, J. et al. Observation of the Dirac fluid and the breakdown of the Wiedemann-Franz law in graphene. *Science* **351**, 1058–1061 (2016).
21. Moll, P. J. W. et al. Evidence for hydrodynamic electron flow in $PdCoO_2$. *Science* **351**, 1061–1064 (2016).
22. Levitov, L. & Falkovich, G. Electron viscosity, current vortices and negative nonlocal resistance in graphene. *Nat. Phys.* **12**, 672–676 (2016).
23. Berdyugin, A. I. et al. Measuring Hall viscosity of graphene's electron fluid. *Science* **364**, 162–165 (2019).
24. Yip, S. K. & Sauls, J. A. Nonlinear Meissner effect in CuO superconductors. *Phys. Rev. Lett.* **69**, 2264–2267 (1992).
25. Volovik, G. E. Superconductivity with lines of GAP nodes: density of states in the vortex. *J. Exp. Theor. Phys. Lett.* **58**, 469–473 (1993).
26. Wu, H. & Sauls, J. A. Majorana excitations, spin and mass currents on the surface of topological superfluid ^{3}He-B. *Phys. Rev. B* **88**, 184506 (2013).
27. Anchenko, Y. M. I. & Zil'Berman, L. A. The Josephson effect in small tunnel contacts. *J. Exp. Theor. Phys.* **55**, 2395–2402 (1969).
28. Ingold, G.-L., Grabert, H. & Eberhardt, U. Electron-pair current through ultrasmall Josephson junctions. *Phys. Rev. B* **50**, 395–402 (1994).
29. Naaman, O., Teizer, W. & Dynes, R. C. Fluctuation dominated Josephson tunneling with a scanning tunneling microscope. *Phys. Rev. Lett.* **87**, 097004 (2001).
30. Fulde, P. in *Tunneling Phenomena in Solids* (eds Burstein, E. & Lundqvist, S.) Ch. 29 (Springer, 1969).

Methods

A custom-built SJTM instrument with a base temperature of ~290 mK is used to measure high-quality $NbSe_2$ single crystals (HQ Graphene). SPECS Nanonis electronics are used for data acquisition protocols. Crystals are cleaved in situ in cryogenic ultra-high vacuum at ~4.2 K and immediately inserted into the STM head. To create the superconductive vortices, a magnetic field of 50 mT (unless otherwise noted) is applied normal to the crystal surface. The superconducting Nb tips are prepared by field emission of a fine Nb wire on a Nb target. Topographic images, $T_P(\mathbf{r},V)$, are acquired in constant-current mode under a sample bias of V. Differential tunnelling conductance images are acquired using a lock-in amplifier (Stanford Research SR830) with a bias modulation of 50 μV. Detailed theoretical analysis and modelling procedures are given in Supplementary Notes 1–7.

Data availability

All data are available in the main text, in the Supplementary Information and on Zenodo[31]. Additional information is available from the corresponding author upon reasonable request.

Code availability

The data analysis computer codes used in this study are available from the corresponding author upon reasonable request.

References

31. Liu, X., Chong, Y. X., Sharma, R. & Davis, J. C. S. Data associated with 'Atomic-scale visualization of electronic fluid flow'. *Zenodo* https://doi.org/10.5281/zenodo.5048540 (2021).

Acknowledgements

We thank J. E. Hoffman, H. Suderow and Z. Hadzibabic for helpful discussions and advice. X.L. acknowledges support from the Kavli Institute at Cornell. X.L., Y.X.C., R.S. and J.C.S.D. acknowledge support from the Moore Foundation's EPiQS Initiative through grant GBMF9457. J.C.S.D. acknowledges support from the Royal Society through award R64897, from Science Foundation Ireland under award SFI 17/RP/5445 and from the European Research Council under award DLV-788932.

Author contributions

X.L and Y.X.C. carried out the experiments. X.L., Y.X.C. and R.S. developed and implemented the analysis. J.C.S.D. conceived and directed the project. The paper reflects the contributions and ideas of all authors.

Competing interests

The authors declare no competing interests.

Additional information

Supplementary information The online version contains supplementary material available at https://doi.org/10.1038/s41563-021-01077-1.

Correspondence and requests for materials should be addressed to J.C.S.D.

Peer review information *Nature Materials* thanks Wei Guo and the other, anonymous, reviewer(s) for their contribution to the peer review of this work.

Reprints and permissions information is available at www.nature.com/reprints.